Nodal-line transition induced Landau gap in strained lattices

Han Cai [1,2,*] Shaojie Ma [3] and Da-Wei Wang [2,4,5]

[1] *College of Optical Science and Engineering, Zhejiang University, Hangzhou 310027, China*

[2] *Interdisciplinary Center for Quantum Information, State Key Laboratory of Extreme Photonics and Instrumentation, and Zhejiang Province Key Laboratory of Quantum Technology and Device, School of Physics, Zhejiang University, Hangzhou 310027, China*

[3] *Department of Optical Science and Engineering, Fudan University, Shanghai 200433, China*

[4] *Hefei National Laboratory, Hefei 230088, China*

[5] *CAS Center for Excellence in Topological Quantum Computation, University of Chinese Academy of Sciences, Beijing 100190, China*

(Received 14 March 2023; revised 16 June 2023; accepted 26 July 2023; published 10 August 2023)

In topological semimetals, the bands can cross at points or lines with different dimensionality and connectivity in momentum space. For graphene and other systems hosting zero-dimensional band touching points, inhomogeneous strain is used to shift the nodal points to mimic gauge fields, whereas the one-dimensional nodal lines can transit between topologically distinct structures in strain fields. Such a nodal-line transition can provide a powerful way to engineer the electronic properties. Here we study the strain-induced Landau quantization for diamond lattices, where nodal chains split into separate lines. The nodal-line transition opens a finite Landau gap for the critical chain point with a vanishing Fermi velocity, which is impossible to be opened in the scenario of magnetic fields or nodal-point systems. Besides the unconventional energy quantization near the chain point, the strained diamond lattices exhibit perfect flat bands in three dimensions with a $\sqrt{n}$-scaling (n is an integer). We also investigate the associated edge states and the line-dependent Hall response. Our work provides an avenue towards understanding the profound roles of nodal-line transition in topological matter and paves the way to study the interplay between strain and higher-dimensional nodal manifolds in arbitrary dimensions.

DOI: 10.1103/PhysRevB.108.085113

I. INTRODUCTION

The graphene [1,2] and Dirac/Weyl semimetals [3–12] host nodal point degeneracy between Bloch bands. The low-energy excitations not only provide a platform to simulate the long-sought models in particle theory, but also open a new era of quantum materials [13–15]. However, the quasiparticles of solid state systems are not limited by the models in high-energy physics [16–19], which significantly enriches the family of topological matter [20–23]. Among those exotic models, the nodal line (NL) [24,25] is a high-dimensional generalization, which can be viewed as a set of nodal points in its transverse plane perpendicular to the line.

NLs are classified as the same structural class [26–28] if they can be continuously transformed into each other without breaking or crossing. A NL can form a closed ring [29–37] or twist with itself to form a knot [38–40]. With more NLs being involved, they can link with each other [41–46] or intersect at a chain point as nodal chains [47–51]. Such complexity is the origin of many exotic properties of NLs, but is rarely explored in the strain engineering so far [36,37]. Initially proposed in graphene, spatially varying the hopping strengths by straining lattices is used to shift the nodal points in momentum space [52–54], which has a similar effect of a vector potential. Such a pseudovector potential (PVP) can lead to a uniform pseudomagnetic field (PMF) and Landau levels in nodal-point systems [55–75]. Since the lattice parameter and symmetry [20–23] are essential for the stability of NLs, inhomogeneous strain can lift the line degeneracy, e.g., reducing the Kramers nodal lines [76] to Weyl points [19] or induce the transition between different NL classes, e.g., breaking a chain into two separate lines [26,49–51], as schematically shown in Fig. 1. The consequence of the latter transition, which is referred to nodal-line transition (NLT), remains elusive.

Here we study the strain engineering of a three-dimensional (3D) diamond lattice hosting nodal chains [77,78], where the strain-induced NLT plays a key role in forming completely flat Landau levels in three dimensions. The same Landau gap is opened for the whole chain, even at the chain point with a zero Fermi velocity, which has no counterpart for magnetic fields or strained nodal-point systems [47,79]. Besides the chain point, we show the PMF preserves the time-reversal symmetry for the nodal chain, thus the associated Hall response can be considered as a generalization of the valley Hall response in strained graphene [55]. Furthermore, we discuss a systematic approach to investigate the strain-induced nodal-manifold transition in hyperdiamond lattices in arbitrary dimensions [80,81].

II. MODEL

The tight-binding Hamiltonian of a diamond lattice is [82]

$$H = \sum_{\boldsymbol{r}} \sum_{j=1}^{4} t_j a_{\boldsymbol{r}}^{\dagger} b_{\boldsymbol{r}+\boldsymbol{\delta}_j} + \text{H.c.}, \tag{1}$$

*hancai@zju.edu.cn

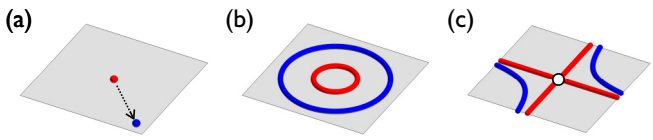

FIG. 1. (a) A nodal point shifts. (b) A nodal ring deforms without NLT. (c) A nodal chain splits into two separate curves at the chain (white) point with NLT.

where t_j ($j = 1, 2, 3, 4$) is the hopping strength between an a-sublattice site at position $\boldsymbol{r}$ to its nearest-neighbor b-sublattice site at position $\boldsymbol{r} + \boldsymbol{\delta}_j$ where $\boldsymbol{\delta}_1 = 1/2(1, -1, -1)$, $\boldsymbol{\delta}_2 = 1/2(-1, 1, -1)$, $\boldsymbol{\delta}_3 = 1/2(-1, -1, 1)$, and $\boldsymbol{\delta}_4 = 1/2(1, 1, 1)$. The Bloch wave vectors of the zero-energy states are obtained according to the condition

$$\sum_{j=1}^{4} t_j e^{-i\boldsymbol{\delta}_j \cdot \boldsymbol{k}} = 0. \tag{2}$$

For the unstrained lattice ($t_j = t$), the energy gap closes along equal-energy lines connecting high symmetry points on the boundary of the Brillouin zone in Fig. 2(a). The topological invariant of NLs is the Berry phase along the path encircling them, which is π for the path around one NL (the dashed circle) and 0 for the path around the chain point enclosing two NLs (the solid circle) [22,49]. Focusing on the plane $k_z = \pi$, the low-energy effective Hamiltonian $H_{1(2)}$ for the NLs along $k_{y(x)}$ are

$$H_1(k_y) = v(k_y)\sigma_2 q_x + w(k_y)\sigma_1 q_z,$$
$$H_2(k_x) = v(k_x)\sigma_2 q_y + w(k_x)\sigma_1 q_z, \tag{3}$$

where $\sigma_{1,2}$ are Pauli matrices; $v(k) = 2t\sin(k/2)$ [$w(k) = 2t\cos(k/2)$] is the in-plane (out-of-plane) Fermi velocity; and $q_x = k_x$, $q_y = k_y$, and $q_z = k_z - \pi$ are the relative lattice momenta measured from the nodal point in its transverse plane.

The Fermi velocities are anisotropic ($v \neq w$) except at the W point [Fig. 2(b)]. At the X point, the in-plane Fermi velocity v vanishes, which can be viewed as an extremely squeezed Dirac cone. To avoid confusion, we need to emphasize that the anisotropy is an intrinsic property of the unstrained diamond lattice, instead of being induced by strain fields [83]. Since the Landau levels of H_1 in a magnetic field B_y along the y-axis is determined by Fermi velocities [84]

$$E_{\pm n} = \pm\sqrt{2n|B_y vw|}, \tag{4}$$

with $\sqrt{|vw|} \propto \sqrt{|\sin(k_y)|}$, one may anticipate that the energy spectra always collapse at the chain point $k_y = 0$ [47] (similar for H_2 in a magnetic field along the x-axis). However, as we demonstrate in the following, the Landau gap can be revived owing to the strain-induced NLT.

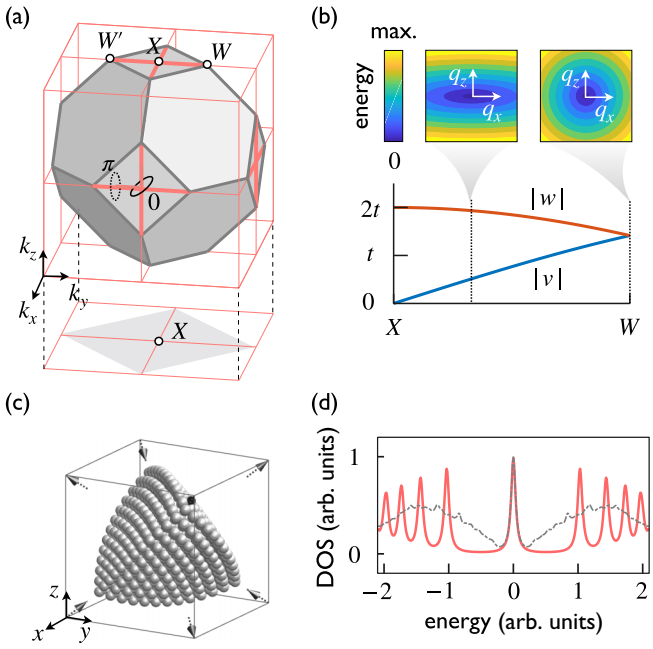

FIG. 2. Nodal chains and quantized energy spectrum. (a) The first Brillouin zone of the diamond lattice and the surface Brillouin zone projected along the z-axis. The zero-energy nodal lines are plotted in red lines connecting high symmetry points. $X(0, 0, \pi)$, $W(0, \pi/2, \pi)$, and $W'(0, -\pi/2, \pi)$. (b) The Fermi velocities along X-W. Insets: The (an)isotropic energy dispersion. (c) The schematic deformation of the a tetrahedral diamond lattice upon a tetraxial strain field. (d) Numerically computed density of states of a strained tetrahedon diamond lattice (3311 sites) exhibits $\sqrt{n}$-scaling energy quantization (red solid line) compared with the unstrained one (purple dashed line). We set the maximum strain constant α (see definition in text) such that all coupling strengths are nonnegative.

III. STRAIN-INDUCED PVP AND PMF

Inspired by the quantum topology of light [77,85], we find that a tetraxial strain $\boldsymbol{u} \propto -(yz, zx, xy)$ (see the Appendix and an alternative derivation in Ref. [78]) can lead to $\sqrt{n}$-scaling discrete energy spectrum in Figs. 2(c) and 2(d), which is the hallmark of Landau quantization of Dirac cones.

Combining Eq. (4) and the quantized energy spectrum, we conclude that the PMF for the NL along k_y is proportional to $\sqrt{1/|\sin(k_y)|}$, which compensates the anisotropic factor of the Fermi velocities $|vw|$ for different points of the NL. In particular, the PMF has to be divergent approaching the chain point X, in stark contrast to nodal-point systems, where the PMF always takes a finite value owing to the constraint of Lifshitz transition [54].

To understand the mechanism of the divergent PMF and associated unconventional quantization, we incorporate the effect of strain field into Hamiltonian in Eq. (1) by modifying the hopping amplitudes [86,87]

$$t_j \to t + \delta t_j = t(1 + \alpha \boldsymbol{r} \cdot \boldsymbol{\delta}_j), \tag{5}$$

which linearly depends on the position $\boldsymbol{r}$ in the weak strain limit $\alpha r \ll 1$. Here α is a strain constant to denote the coupling variation with respect to the position, and we take the assumption that hopping strength correction δt_j varies much more slowly than the lattice constant. Equation (5) can be obtained from a Fock-space quantum optics model owing to the mathematical equivalence (see the Appendix) or directly derived by applying the finite element method to the solid deformation [88]).

It is instructive to locally study the NLs at different positions. Depicting the modified coupling strengths and cor-

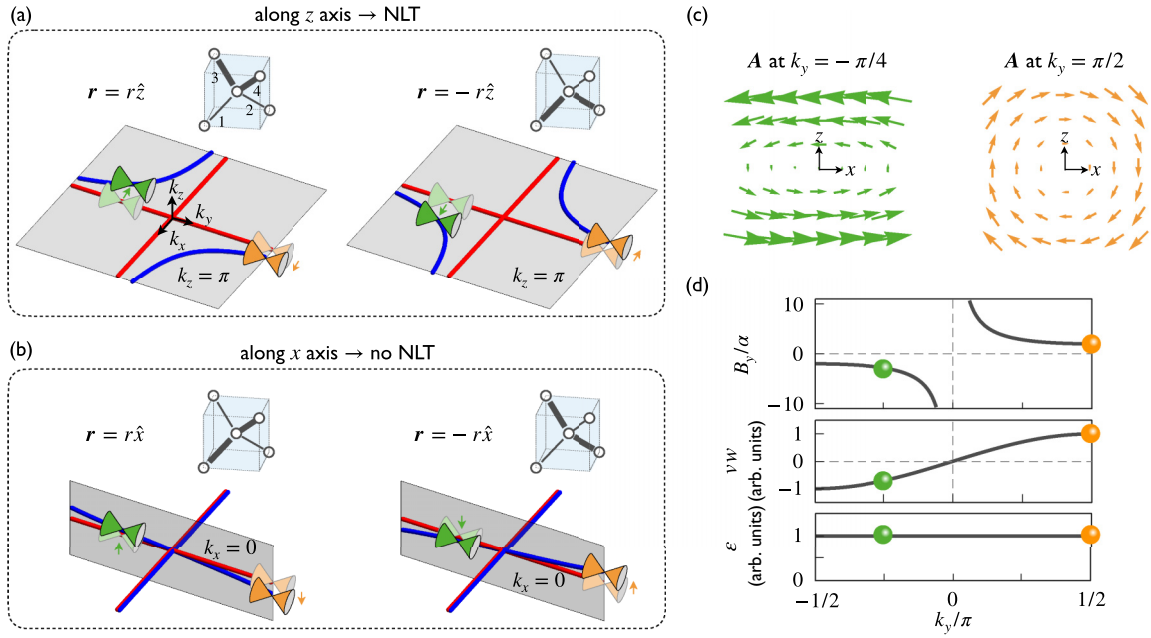

FIG. 3. PVP and PMF for nodal chains. The nodal chain at $k_z = \pi$ (a) splits when $\boldsymbol{r}$ is along the z-axis and (b) preserves when $\boldsymbol{r}$ is along the x-axis. Insets: The hopping strength correction is indicated by the bond width. Blue (red) lines denote the strained (original) zero-energy NLs. (c) The chiral PVP distribution for the nodal points at $k_y = -\pi/4$ [green cones in (b)] and $\pi/2$ [orange cones in (b)]. (d) The PMF, Fermi velocity anisotropicity, and the Landau gap for the NL along k_y (W'-W).

responding NLs, we notice that the nodal chain at $k_z = \pi$ splits when $\boldsymbol{r}$ is along the z-axis [Fig. 3(a)], while the same nodal chain preserves when $\boldsymbol{r}$ is along x-axis [Fig. 3(b)] and y-axis (not shown). To be specific, the bonds $\boldsymbol{\delta}_{1,2}$ are stretched while the bonds $\boldsymbol{\delta}_{3,4}$ are squeezed when $\boldsymbol{r} = r\hat{z}$ with $r = |\boldsymbol{r}|$ and $\hat{i}$ being the unit vector along i-axis. We substitute the coupling strength correction $\delta t_{3,4} = -\delta t_{1,2} = \alpha z/2$ into Eqs. (2) and (5), and obtain two open curves, i.e., the NLT happens [49,51]. One the contrary, the bonds $\boldsymbol{\delta}_{2,3}$ are stretched while the bonds $\boldsymbol{\delta}_{1,4}$ are squeezed when $\boldsymbol{r} = r\hat{x}$. The resultant coupling strength correction $\delta t_{1,4} = -\delta t_{2,3} = \alpha x/2$ slightly deforms and rotates the nodal chain with respect to the x-axis, and preserves the chain point. When $\boldsymbol{r}$ is along the y-axis, the nodal chain similarly rotates with respect to the y-axis. To summerize, we conclude that the chain point at $k_i = \pi$ ($i = x, y, z$) only splits when $\boldsymbol{r}$ is along the i-axis.

The strain effect to the NLs can be considered as each original nodal point being coupled to a PVP $\boldsymbol{A} \equiv (A_x, A_y, A_z)$ in its transverse plane, as schematically illustrated by the cones at $k_y = \pi/2$ (orange) and $k_y = -\pi/4$ (green). For the NL along k_y, we obtain the PVP as a function of $\boldsymbol{r}$ for each nodal point to the first order of αr [88],

$$A_x = \alpha z \cot(k_y/2), \quad A_z = -\alpha x \tan(k_y/2), \tag{6}$$

and $A_y = 0$. The PVPs at $k_y = \pi/2$ and $k_y = -\pi/4$ with opposite chiralities are plotted in Fig. 3(c), enabling us to calculate the PMF $\boldsymbol{B} \equiv (B_x, B_y, B_z)$,

$$B_y(k_y) = \frac{\partial A_x}{\partial z} - \frac{\partial A_z}{\partial x} = \frac{2\alpha}{\sin(k_y)}, \tag{7}$$

and $B_x = B_z = 0$ for the NL along k_y in Fig. 3(d). Such a divergence is unique for NLT because the chain point splitting cannot be described in a smooth way. The associated Landau level energies read $E_{\pm n} = \pm\sqrt{n}\varepsilon$, with $\varepsilon = 2\sqrt{2\alpha t}$ being independent of momentum k_y. Similarly, we can obtain the PMF for the NL along k_x as $B_x(k_x) = -2\alpha/\sin(k_x)$ and $B_y = B_z = 0$ [88].

IV. BAND SPECTRA AND SURFACE STATES

To highlight the physics of NLT, we introduce the stretch types in Fig. 3(a) to the diamond lattice as a uniaxial modulation of the hopping strengths [schematic in Fig. 4(a)]. Since the periodicity in the x-y plane is preserved in such a z-axis modulation, it enables us to obtain the band spectra of the projected surface Brillouin zone Fig. 1(a). Such a uniaxial variation is commonly used to study valley Hall effect and edge states [90–97] in strained graphene.

The PMF for the uniaxially modulated lattices can be obtained by keeping the A_x component in Eq. (6), which fully captures the NLT

$$B'_y(k_y) = \alpha \cot(k_y/2), \tag{8}$$

for the NL along k_y and $B'_x(k_x) = -\alpha \cot(k_x/2)$ for the NL along k_x. The Landau levels for each NL is [Fig. 4(b)]

$$E'_{\pm n}(k_{y(x)}) = \pm\sqrt{n}\varepsilon', \tag{9}$$

with $\varepsilon' = |\cos(k_{y(x)})|\varepsilon$. We notice that the Landau gaps are momentum-dependent with $\varepsilon' = \varepsilon$ at the X point, indicating the unconventional Landau quantization of the chain point X is solely contributed by the NLT.

Furthermore, the band spectra enable us to analyze the direction of PMF. In Fig. 4(c), we numerically compute the band spectra along the transverse plane of the nodal points $k_y = \pm\pi/3$ and $2\pi/3$, where the color indicates the expectation value of the z position operator for each eigenstate.

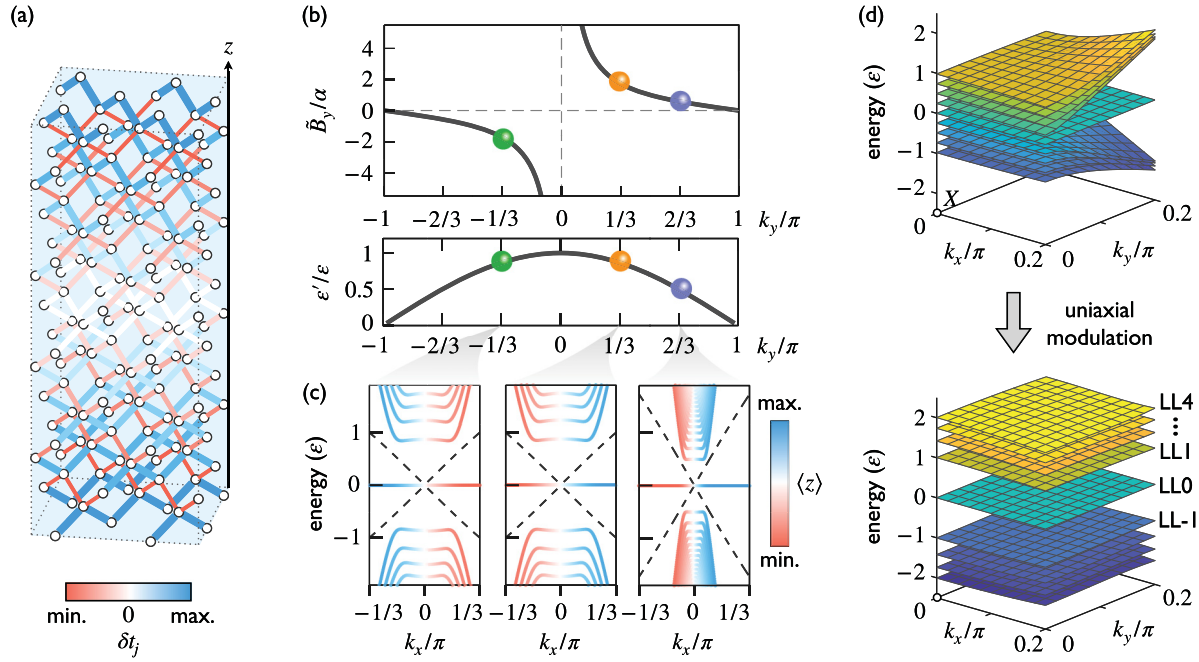

FIG. 4. Band spectra and surface states. (a) The schematic of a diamond lattice with a uniaxial modulated hopping strengths. The color and width of the bonds scales the coupling strength correction. (b) The PMF and Landau gap. (c) The exact diagonalization of the band spectra along the transverse plane of the NL along k_y, where the locking between the edge mode dispersion and surface determines the PMF direction. The dashed lines indicates the unstrained Dirac cones. (d) The numerically computed Landau levels (LLs) near the chain point X. In the numerical simulation, the lattice contains 201 layers along the z-axis and the maximum coupling strength correction is set to be $0.2t$.

For each panel, the flat Landau levels and bending edges are reminiscent of the integer quantum Hall effect, where the locking between the band dispersion and top/bottom surface determines the PMF direction. For example, an excitation at $k_y = -\pi/3$ can merge into the edge mode on the bottom surface when a weak electric field adiabatically increases the momentum k_x. The Hall drift [84] gives the direction of the PMF

$$\boldsymbol{B}' \propto \hat{z} \times \nabla_{\boldsymbol{k}} \langle z \rangle, \tag{10}$$

which is along the negative y-axis at $k_y = -\pi/3$. On the contrary, the gradient $\partial\langle z\rangle/\partial k_x > 0$ for the time-reversal point at $k_y = \pi/3$ indicates a PMF in the opposite direction. Remarkably, the NL Hall response is an intrinsic 3D phenomenon, which vanishes in the reduction of the slab thickness.

Finally, the Landau levels at $k_y = \pi/3, 2\pi/3$ also confirm the Landau quantization energy in Eq. (9). In Fig. 4(d), we numerically compute the band spectra before and after the uniaxial modulation.

V. HYPERDIAMOND LATTICES IN ARBITRARY DIMENSIONS

Our results can be generalized to d-dimensional (dD) hyperdiamond lattices [80,81]. The Hamiltonian $H_d = \sum_{\boldsymbol{r}} \sum_{j=1}^{d+1} t_j a_{\boldsymbol{r}}^\dagger b_{\boldsymbol{r}+\boldsymbol{\delta}_j} + \text{H.c.}$, where each a-sublattice site is connected to $d+1$ b-sublattice sites with $\boldsymbol{\delta}_i \cdot \boldsymbol{\delta}_j/(|\boldsymbol{\delta}_i||\boldsymbol{\delta}_j|) = -1/d$ $(i \neq j)$. It can be proved that the energy spectra of the dD hyperdiamond lattices are quantized to form dD flat levels by introducing Eq. (5) with $j = 1, \ldots, d+1$, e.g., a five-axial "strain" for four-dimensional (4D) hyperdiamond lattices. Similar to the derivation in three dimensions, such a hopping strength correction is adopted from the dD Fock-state lattices [77,85,98–100] whose quantized energy spectra are analytically solved by the $(d+1)$-mode Jaynes-Cummings model. Furthermore, we can obtain the zero-energy $(d-2)$D nodal-manifold in momentum space according to $\sum_{j=1}^{d+1} t_j e^{-i\boldsymbol{\delta}_j \cdot \boldsymbol{k}} = 0$. By comparing the nodal manifolds for original and strained lattices, we can investigate the nodal-manifold transition between different structural classes and resultant manifold-dependent Hall response.

In conclusion, we show that the strain-induced NLT is a novel and powerful mechanism to design the energy spectra of nodal-line semimetals. In general, the response of NLs to strain fields can be viewed as each nodal point being shifted within the two-dimensional (2D) plane perpendicular to the line direction, resulting in the PMF with a line-dependent strength, respectively. For the chain point, its breaking effectively moves the point to infinity. Therefore, the divergent PMF can open a finite Landau gap at the critical point, without analogues in nodal-point systems or magnetic fields. Our result demonstrates that the an intrinsic 3D Hall response which cannot be treated as a sum of quasi-two-dimensional contribution [101]. The strain engineering of flat Landau levels in three dimensions [37] is ready to be generalized to arbitrary dimensions, which provides an opportunity for studying strong correlated topological phases in higher dimensions [102,103]. The corresponding phenomena are ready to be tested in higher-dimensional electric circuits [104–106] and acoustic resonator array [107,108]. In applications, the NL Hall response can be used to design a momentum filter, which provides more control knobs beyond valleys [109–113].

ACKNOWLEDGMENTS

This work was supported by the National Natural Science Foundation of China (Grant No. U21A20437), the National Key Research and Development Program of China (Grant No. 2019YFA0308100), Zhejiang Province Key Research and Development Program (Grant No. 2020C01019), Innovation Program for Quantum Science and Technology (Grant No. 2021ZD0303200), the Strategic Priority Research Program of Chinese Academy of Sciences (Grant No. XDB28000000), and the Fundamental Research Funds for the Central Universities.

APPENDIX: DERIVATION OF EQ. (5) FROM A QUANTUM OPTICS MODEL

We start from the four-mode Jaynes-Cummings model (we set $\hbar = 1$)

$$H_{JC} = \frac{\omega}{2}s_z + \sum_{j=1}^{4} \nu c_j^\dagger c_j + \sum_{j=1}^{4}[g(c_j^\dagger + c_j)(s_+ + s_-) + \text{H.c.}],$$

where $s_+ = s_-^\dagger = |\uparrow\rangle\langle\downarrow|$ and $s_z = s_+s_- - s_-s_+$ are the raising and lowering operators and the z-component of the Pauli matrices of the two atomic levels with the transition frequency ω, $c_j(c_j^\dagger)$ is the annihilation (creation) operator of the jth cavity mode with resonance frequency ν, and g is the coupling strength between the atom and the cavities, as shown in Fig. 5(a). We assume that the frequency of the cavities is on-resonant with the transition frequency of the atom $\nu = \omega$. With the rotating-wave approximation, the Hamiltonian in the interaction picture is

$$H_{JC} = g\sum_{j=1}^{4} c_j^\dagger s_- + \text{H.c.}. \tag{A1}$$

Since the Hamiltonian H_{JC} in Eq. (A1) commutes with the sum of atomic excitation and photons $N = \sum_j c_j^\dagger c_j + |\uparrow\rangle\langle\uparrow|$, the subspaces with different N are decoupled and can be studied individually [Fig. 5(b)]

The N-excitation subspace contains $(2N+3)(N+2)(N+1)/6$ Fock states $|\uparrow/\downarrow; n_1, n_2, n_3, n_4\rangle$ satisfying $q + \sum_j n_j = N$, where the nonnegative integer n_j is the photon number in the jth cavity mode, $q = 0$ for the atomic ground state $|\downarrow\rangle$, and $q = 1$ for the excited state $|\uparrow\rangle$. These Fock states constitute 3D tight-binding diamond lattice, where $|\uparrow; n_1, n_2, n_3, n_4\rangle$ is coupled to $|\downarrow; n_1+1, n_2, n_3, n_4\rangle$, $|\downarrow; n_1, n_2+1, n_3, n_4\rangle$, $|\downarrow; n_1, n_2, n_3+1, n_4\rangle$, and $|\downarrow; n_1, n_2, n_3, n_4+1\rangle$ with Rabi frequency proportional to $\sqrt{n_1+1}$, $\sqrt{n_2+1}$, $\sqrt{n_3+1}$, and $\sqrt{n_4+1}$, respectively. Hence the hopping strength between two neighboring Fock states is

$$t_j = g\sqrt{n_j + 1}, \tag{A2}$$

which is owing to the nature of the bosonic annihilation operator, i.e., $c|p\rangle = \sqrt{p}|p-1\rangle$.

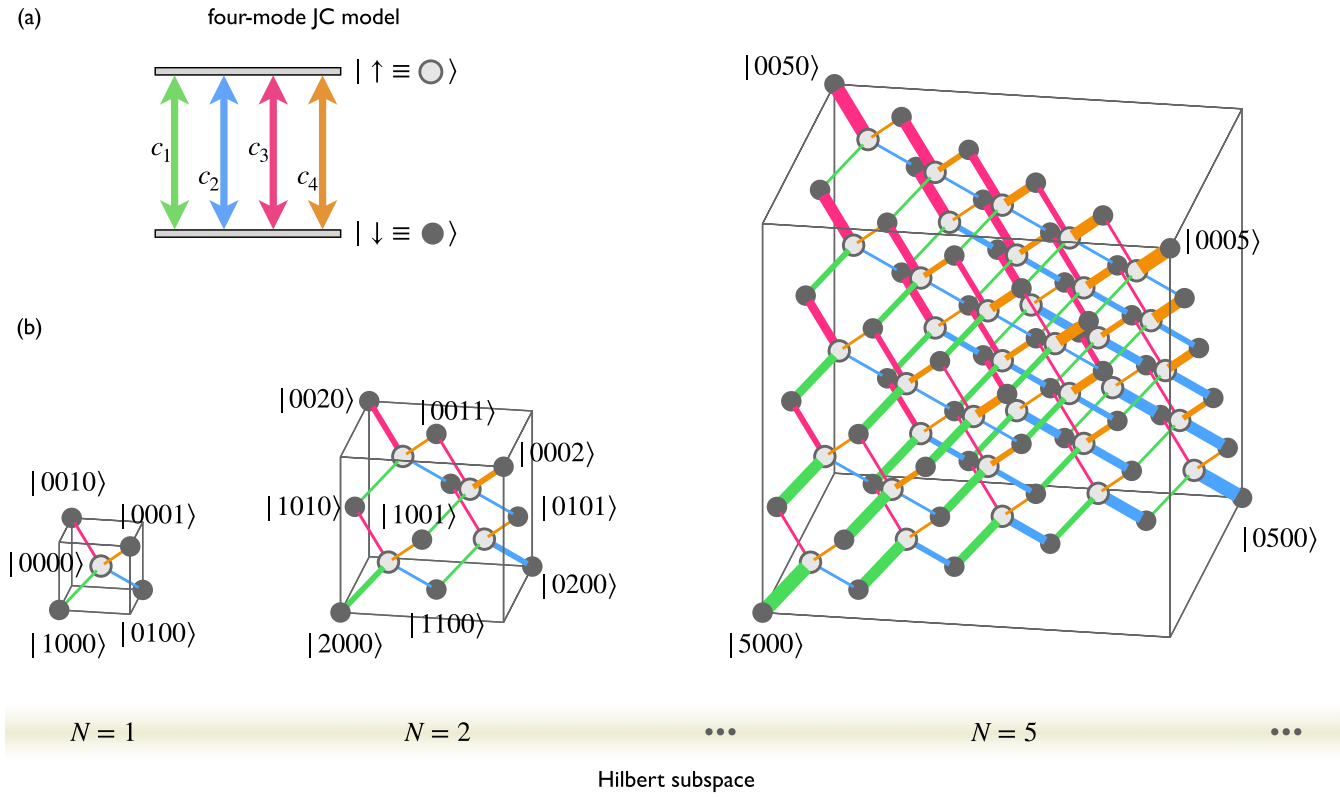

FIG. 5. (a) Four-mode Jaynes-Cummings model: a two-level atom coupled with four cavity modes. (b) The 3D FSLs with different N. The empty (filled) balls denote the atomic states $|\uparrow\rangle$ ($|\downarrow\rangle$). The green, blue, red, and orange bonds between adjacent Fock states describe the coupling between the cavity mode c_j ($j = 1, 2, 3, 4$), respectively. The square-root-scaling coupling strengths (Rabi frequencies) are indicated by the bond widths.

The eigenstates of the 3D Fock-state lattices [77,85] (FSL) can be solved analytically by introducing the collective modes with annihilation operators $b_j = 1/2\sum_{n=1}^{4} c_n e^{inj\pi/2}$ ($j = 0, 1, 2, 3$), respectively. With the collective modes, the Hamiltonian in Eq. (A1) can be reduced to a single-mode Jaynes-Cummings (JC) model

$$H_{\mathrm{JC}} = 2gb_0^{\dagger}\sigma_- + \mathrm{H.c.},$$

where the atom only couples the mode b_0. Therefore, the eigenspectrum

$$E_m = 2g\sqrt{m}, \tag{A3}$$

is quantized with square-root-scaling, where m is the photon number in b_0 mode.

In mapping the Fock space of the JC model to a tight-binding diamond lattice with tetrahedral boundary, each Fock state $|\downarrow; n_1, n_2, n_3, n_4\rangle$ can be assigned to a site with $x = (n_1 - n_2 - n_3 + n_4)/2$, $y = (-n_1 + n_2 - n_3 + n_4)/2$, and $z = (-n_1 - n_2 + n_3 + n_4)/2$. Together with the constraint $n_1 + n_2 + n_3 + n_4 = N$, we obtain the position $n_j = (\boldsymbol{r}\cdot\boldsymbol{\delta}_j + N/4)$. Therefore, the hopping strength in Eq. (A2) near the center of the FSL is (we assume $n_j \approx N/4 \gg 1$)

$$t_j \approx g\sqrt{n_j} \approx t(1 + \alpha\boldsymbol{r}\cdot\boldsymbol{\delta}_j),$$

with $t = g\sqrt{N}/2$ and $\alpha = 2/N$. The $\sqrt{N}$-scaling in the mapping of the hopping strength has a physical origin. For real systems, the characteristic energy is determined by the hopping strength t, which is independent on the system size. However, the energy spectrum of Fock-state lattices [Eq. (A3)] is scaled with respect to the total excitation number $\propto\sqrt{N}$. Therefore, we need to set $g\sqrt{N}$ as a constant in this mapping.

[1] K. S. Novoselov, A. K. Geim, S. V. Morozov, D. Jiang, M. I. Katsnelson, I. V. Grigorieva, S. V. Dubonos, and A. A. Firsov, Two-dimensional gas of massless Dirac fermions in graphene, Nature (London) **438**, 197 (2005).

[2] Y. Zhang, Y. W. Tan, H. L. Storner, and P. Kim, Experimental observation of the quantum Hall effect and Berry's phase in graphene, Nature (London) **438**, 201 (2005).

[3] X. Wan, A. M. Turner, A. Vishwanath, and S. Y. Savrasov, Topological semimetal and Fermi-arc surface states in the electronic structure of pyrochlore iridates, Phys. Rev. B **83**, 205101 (2011).

[4] A. A. Burkov and L. Balents, Weyl Semimetal in a Topological Insulator Multilayer, Phys. Rev. Lett. **107**, 127205 (2011).

[5] S. M. Young, S. Zaheer, J. C. Y. Teo, C. L. Kane, E. J. Mele, and A. M. Rappe, Dirac Semimetal in Three Dimensions, Phys. Rev. Lett. **108**, 140405 (2012).

[6] Z. Wang, Y. Sun, X. Q. Chen, C. Franchini, G. Xu, H. Weng, X. Dai, and Z. Fang, Dirac semimetal and topological phase transitions in A3Bi (A = Na, K, Rb), Phys. Rev. B **85**, 195320 (2012).

[7] Z. K. Liu, B. Zhou, Y. Zhang, Z. J. Wang, H. M. Weng, D. Prabhakaran, S. K. Mo, Z. X. Shen, Z. Fang, X. Dai, Z. Hussain, and Y. L. Chen, Discovery of a three-dimensional topological dirac semimetal, Na_3Bi, Science **343**, 864 (2014).

[8] S. M. Huang, S. Y. Xu, I. Belopolski, C. C. Lee, G. Chang, B. Wang, N. Alidoust, G. Bian, M. Neupane, C. Zhang, S. Jia, A. Bansil, H. Lin, and M. Z. Hasan, A Weyl fermion semimetal with surface Fermi arcs in the transition metal monopnictide TaAs class, Nat. Commun. **6**, 7373 (2015).

[9] H. Weng, C. Fang, Z. Fang, A. Bernevig, and X. Dai, Weyl Semimetal Phase in Noncentrosymmetric Transition-Metal Monophosphides, Phys. Rev. X **5**, 011029 (2015).

[10] S. Y. Xu, I. Belopolski, N. Alidoust, M. Neupane, G. Bian, C. Zhang, R. Sankar, G. Chang, Z. Yuan, C. C. Lee, S. M. Huang, H. Zheng, J. Ma, D. S. Sanchez, B. Wang, A. Bansil, F. Chou, P. P. Shibayev, H. Lin, S. Jia, and M. Z. Hasan, Discovery of a Weyl fermion semimetal and topological Fermi arcs, Science **349**, 613 (2015).

[11] B. Q. Lv, H. M. Weng, B. B. Fu, X. P. Wang, H. Miao, J. Ma, P. Richard, X. C. Huang, L. X. Zhao, G. F. Chen, Z. Fang, X. Dai, T. Qian, and H. Ding, Experimental Discovery of Weyl Semimetal TaAs, Phys. Rev. X **5**, 031013 (2015).

[12] L. Lu, Z. Wang, D. Ye, L. Ran, L. Fu, J. D. Joannopoulos, and M. Soljačić, Experimental observation of Weyl points, Science **349**, 622 (2015).

[13] A. H. Castro Neto, F. Guinea, N. M. R. Peres, K. S. Novoselov, and A. K. Geim, The electronic properties of graphene, Rev. Mod. Phys. **81**, 109 (2009).

[14] M. Z. Hasan and C. L. Kane, Topological insulators, Rev. Mod. Phys. **82**, 3045 (2010).

[15] X. L. Qi and S. C. Zhang, Topological insulators and superconductors, Rev. Mod. Phys. **83**, 1057 (2011).

[16] A. A. Soluyanov, D. Gresch, Z. Wang, Q. Wu, M. Troyer, X. Dai, and B. A. Bernevig, Type-II Weyl semimetals, Nature (London) **527**, 495 (2015).

[17] Y. Xu, F. Zhang, and C. Zhang, Structured Weyl Points in Spin-Orbit Coupled Fermionic Superfluids, Phys. Rev. Lett. **115**, 265304 (2015).

[18] B. Bradlyn, J. Cano, Z. Wang, M. G. Vergniory, C. Felser, R. J. Cava, and B. A. Bernevig, Beyond Dirac and Weyl fermions: Unconventional quasiparticles in conventional crystals, Science **353**, aaf5037 (2016).

[19] G. Chang, B. J. Wieder, F. Schindler, D. S. Sanchez, I. Belopolski, S. M. Huang, B. Singh, D. Wu, T. R. Chang, T. Neupert, S. Y. Xu, H. Lin, and M. Z. Hasan, Topological quantum properties of chiral crystals, Nat. Mater. **17**, 978 (2018).

[20] C. K. Chiu, J. C. Y. Teo, A. P. Schnyder, and S. Ryu, Classification of topological quantum matter with symmetries, Rev. Mod. Phys. **88**, 035005 (2016).

[21] B. Q. Lv, T. Qian, and H. Ding, Experimental perspective on three-dimensional topological semimetals, Rev. Mod. Phys. **93**, 025002 (2021).

[22] M. Z. Hasan, G. Chang, I. Belopolski, G. Bian, S. Y. Xu, and J. X. Yin, Weyl, Dirac and high-fold chiral fermions in topological quantum matter, Nat. Rev. Mater. **6**, 784 (2021).

[23] B. J. Wieder, B. Bradlyn, J. Cano, Z. Wang, M. G. Vergniory, L. Elcoro, A. A. Soluyanov, C. Felser, T. Neupert, N. Regnault, and B. A. Bernevig, Topological materials dis-

covery from crystal symmetry, Nat. Rev. Mater. **7**, 196 (2021).
[24] A. A. Burkov, M. D. Hook, and L. Balents, Topological nodal semimetals, Phys. Rev. B **84**, 235126 (2011).
[25] T. T. Heikkilä and G. E. Volovik, Dimensional crossover in topological matter: Evolution of the multiple Dirac point in the layered system to the flat band on the surface, JETP Lett. **93**, 59 (2011).
[26] Z. Yang, C. K. Chiu, C. Fang, and J. Hu, Jones Polynomial and Knot Transitions in Hermitian and non-Hermitian Topological Semimetals, Phys. Rev. Lett. **124**, 186402 (2020).
[27] H. Hu and E. Zhao, Knots and Non-Hermitian Bloch Bands, Phys. Rev. Lett. **126**, 010401 (2021).
[28] H. Park, W. Gao, X. Zhang, and S. S. Oh, Nodal lines in momentum space: Topological invariants and recent realizations in photonic and other systems Nanophotonics **11**, 2779 (2022).
[29] C. Fang, Y. Chen, H. Y. Kee, and L. Fu, Topological nodal line semimetals with and without spin-orbital coupling Phys. Rev. B **92**, 081201(R) (2015).
[30] Y. Chen, Y. Xie, S. A. Yang, H. Pan, F. Zhang, M. L. Cohen, and S. Zhang, Nanostructured carbon allotropes with weyl-like loops and points, Nano Lett. **15**, 6974 (2015).
[31] K. Mullen, B. Uchoa, and D. T. Glatzhofer, Line of Dirac Nodes in Hyperhoneycomb Lattices, Phys. Rev. Lett. **115**, 026403 (2015).
[32] Y. Kim, B. J. Wieder, C. L. Kane, and A. M. Rappe, Dirac Line Nodes in Inversion-Symmetric Crystals, Phys. Rev. Lett. **115**, 036806 (2015).
[33] R. Yu, H. Weng, Z. Fang, X. Dai, and X. Hu, Topological Node-Line Semimetal and Dirac Semimetal State in Antiperovskite Cu3PdN, Phys. Rev. Lett. **115**, 036807 (2015).
[34] J. W. Rhim and Y. B. Kim, Landau level quantization and almost flat modes in three-dimensional semimetals with nodal ring spectra, Phys. Rev. B **92**, 045126 (2015).
[35] W. Deng, J. Lu, F. Li, X. Huang, M. Yan, J. Ma, and Z. Liu, Nodal rings and drumhead surface states in phononic crystals, Nat. Commun. **10**, 1769 (2019).
[36] S. W. Kim and B. Uchoa, Elastic gauge fields and zero-field three-dimensional quantum Hall effect in hyperhoneycomb lattices, Phys. Rev. B **99**, 201301(R) (2019).
[37] A. Lau, T. Hyart, C. Autieri, A. Chen, and D. I. Pikulin, Designing Three-Dimensional Flat Bands in Nodal-Line Semimetals, Phys. Rev. X **11**, 031017 (2021).
[38] M. Ezawa, Topological semimetals carrying arbitrary Hopf numbers: Fermi surface topologies of a Hopf link, Solomon's knot, trefoil knot, and other linked nodal varieties, Phys. Rev. B **96**, 041202(R) (2017).
[39] R. Bi, Z. Yan, L. Lu, and Z. Wang, Nodal-knot semimetals, Phys. Rev. B **96**, 201305(R) (2017).
[40] C. H. Lee, A. Sutrisno, T. Hofmann, T. Helbig, Y. Liu, Y. S. Ang, L. K. Ang, X. Zhang, M. Greiter, and R. Thomale, Imaging nodal knots in momentum space through topolectrical circuits, Nat. Commun. **11**, 4385 (2020).
[41] W. Chen, H. Z. Lu, and J. M. Hou, Topological semimetals with a double-helix nodal link, Phys. Rev. B **96**, 041102(R) (2017).
[42] Z. Yan, R. Bi, H. Shen, L. Lu, S.-C. Zhang, and Z. Wang, Nodal-link semimetals, Phys. Rev. B **96**, 041103(R) (2017).
[43] G. Chang, S. Y. Xu, X. Zhou, S. M. Huang, B. Singh, B. Wang, I. Belopolski, J. Yin, S. Zhang, A. Bansil, H. Lin, and M. Z. Hasan, Topological Hopf and Chain Link Semimetal States and Their Application to Co_2MnGa, Phys. Rev. Lett. **119**, 156401 (2017).
[44] Q. Wu, A. A. Soluyanov, and T. Bzdušek, Non-abelian band topology in noninteracting metals, Science **365**, 1273 (2019).
[45] E. Yang, B. Yang, O. You, H. C. Chan, P. Mao, Q. Guo, S. Ma, L. Xia, D. Fan, Y. Xiang, and S. Zhuang, Observation of Non-Abelian Nodal Links in Photonics, Phys. Rev. Lett. **125**, 033901 (2020).
[46] H. Park, S. Wong, X. Zhang, and S. S. Oh, Non-abelian charged nodal links in a dielectric photonic crystal, ACS Photonics **8**, 2746 (2021).
[47] T. Bzdušek, Q. Wu, A. Rüegg, M. Sigrist, and A. A. Soluyanov, Nodal-chain metals, Nature (London) **538**, 75 (2016).
[48] R. Yu, Q. Wu, Z. Fang, and H. Weng, From Nodal Chain Semimetal to Weyl Semimetal in HfC, Phys. Rev. Lett. **119**, 036401 (2017).
[49] Q. Yan, R. Liu, Z. Yan, B. Liu, H. Chen, Z. Wang, and L. Lu, Experimental discovery of nodal chains, Nat. Phys. **14**, 461 (2018).
[50] J. Lu, X. Huang, M. Yan, F. Li, W. Deng, and Z. Liu, Nodal-Chain Semimetal States and Topological Focusing in Phononic Crystals, Phys. Rev. Appl. **13**, 054080 (2020).
[51] D. Wang, B. Yang, Q. Guo, R. Y. Zhang, L. Xia, X. Su, W. J. Chen, J. Han, S. Zhang, and C. T. Chan, Intrinsic in-plane nodal chain and generalized quaternion charge protected nodal link in photonics, Light Sci. Appl. **10**, 83 (2021).
[52] H. Suzuura and T. Ando, Phonons and electron-phonon scattering in carbon nanotubes, Phys. Rev. B **65**, 235412 (2002).
[53] J. L. Mañes, Symmetry-based approach to electron-phonon interactions in graphene, Phys. Rev. B **76**, 045430 (2007).
[54] V. M. Pereira, A. H. Castro Neto, and N. M. R. Peres, Tight-binding approach to uniaxial strain in graphene, Phys. Rev. B **80**, 045401 (2009).
[55] F. Guinea, M. I. Katsnelson, and A. K. Geim, Energy gaps and a zero-field quantum Hall effect in graphene by strain engineering, Nat. Phys. **6**, 30 (2010).
[56] N. Levy, S. A. Burke, K. L. Meaker, M. Panlasigui, A. Zettl, F. Guinea, A. H. Castro Neto, and M. F. Crommie, Strain-induced pseudomagnetic fields greater than 300 tesla in graphene nanobubbles, Science **329**, 544 (2010).
[57] K. K. Gomes, W. Mar, W. Ko, F. Guinea, and H. C. Manoharan, Designer Dirac fermions and topological phases in molecular graphene, Nature (London) **483**, 306 (2012).
[58] M. C. Rechtsman, J. M. Zeuner, A. Tünnermann, S. Nolte, M. Segev, and A. Szameit, Strain-induced pseudomagnetic field and photonic Landau levels in dielectric structures, Nat. Photon. **7**, 153 (2013).
[59] M. Neek-Amal, L. Covaci, Kh. Shakouri, and F. M. Peeters, Electronic structure of a hexagonal graphene flake subjected to triaxial stress, Phys. Rev. B **88**, 115428 (2013).
[60] W. Yan, W. Y. He, Z. D. Chu, M. Liu, L. Meng, R. F. Dou, Y. Zhang, Z. Liu, J. C. Nie, and L. He, Strain and curvature induced evolution of electronic band structures in twisted graphene bilayer, Nat. Commun. **4**, 2159 (2013).

[61] G. J. Verbiest, S. Brinker, and C. Stampfer, Uniformity of the pseudomagnetic field in strained graphene, Phys. Rev. B **92**, 075417 (2015).
[62] B. Tian, M. Endres, and D. Pekker, Landau Levels in Strained Optical Lattices, Phys. Rev. Lett. **115**, 236803 (2015).
[63] M. Settnes, S. R. Power, and A. Jauho, Pseudomagnetic fields and triaxial strain in graphene, Phys. Rev. B **93**, 035456 (2016).
[64] Z. Yang, F. Gao, Y. Yang, and B. Zhang, Strain-Induced Gauge Field and Landau Levels in Acoustic Structures, Phys. Rev. Lett. **118**, 194301 (2017).
[65] Y. Liu, J. N. B. Rodrigues, Y. Z. Luo, L. Li, A. Carvalho, M. Yang, E. Laksono, J. Lu, Y. Bao, H. Xu, S. J. R. Tan, Z. Qiu, C. H. Sow, Y. P. Feng, A. H. Castro Neto, S. Adam, J. Lu, and K. P. Loh, Tailoring sample-wide pseudo-magnetic fields on a graphene-black phosphorus heterostructure, Nat. Nanotechnol. **13**, 828 (2018).
[66] P. Nigge, A. C. Qu, É. Lantagne-Hurtubise, E. Mårsell, S. Link, G. Tom, M. Zonno, M. Michiardi, M. Schneider, S. Zhdanovich, G. Levy, U. Starke, C. Gutièrrez, D. Bonn, S. A. Burke, M. Franz, and A. Damascelli, Room temperature strain-induced Landau levels in graphene on a wafer-scale platform, Sci. Adv. **5**, eaaw5593 (2019).
[67] C. C. Hsu, M. L. Teague, J. Q. Wang, and N. C. Yeh, Nanoscale strain engineering of giant pseudo-magnetic fields, valley polarization, and topological channels in graphene, Sci. Adv. **6**, eaat9488 (2020).
[68] O. Jamadi, E. Rozas, G. Salerno, M. Milićević, T. Ozawa, I. Sagnes, A. Lemaître, L. Le Gratiet, A. Harouri, I. Carusotto, J. Bloch, and A. Amo, Direct observation of photonic Landau levels and helical edge states in strained honeycomb lattices, Light Sci. Appl. **9**, 144 (2020).
[69] M. Bellec, C. Poli, U. Kuhl, F. Mortessagne, and H. Schomerus, Observation of supersymmetric pseudo-Landau levels in strained microwave graphene, Light Sci. Appl. **9**, 146 (2020).
[70] C. Mann, S. A. R. Horsley, and E. Mariani, Tunable pseudomagnetic fields for polaritons in strained metasurfaces, Nat. Photon. **14**, 669 (2020).
[71] A. Cortijo, Y. Ferreirós, K. Landsteiner, and M. A. H. Vozmediano, Elastic Gauge Fields in Weyl Semimetals, Phys. Rev. Lett. **115**, 177202 (2015).
[72] D. I. Pikulin, A. Chen, and M. Franz, Chiral Anomaly from Strain-Induced Gauge Fields in Dirac and Weyl Semimetals, Phys. Rev. X **6**, 041021 (2016).
[73] A. G. Grushin, W. F. Venderbos, A. Vishwanath, and R. Ilan, Inhomogeneous Weyl and Dirac Semimetals: Transport in Axial Magnetic Fields and Fermi Arc Surface States from Pseudo-Landau Levels, Phys. Rev. X **6**, 041046 (2016).
[74] H. Jia, R. Zhang, W. Gao, Q. Guo, B. Yang, J. Hu, Y. Bi, Y. Xiang, C. Liu, and S. Zhang, Observation of chiral zero mode in inhomogeneous three-dimensional Weyl metamaterials, Science **363**, 148 (2019).
[75] V. Peri, M. Serra-Garcia, R. Ilan, and S. D. Huber, Axial-field-induced chiral channels in an acoustic Weyl system, Nat. Phys. **15**, 357 (2019).
[76] Y. M. Xie, X. J. Gao, X. Y. Xu, C. P. Zhang, J. X. Hu, J. Z. Gao, and K. T. Law, Kramers nodal line metals, Nat. Commun. **12**, 3064 (2021).
[77] H. Cai and D. W. Wang, Topological phases of quantized light, Nat. Sci. Rev. **8**, nwaa196 (2021).
[78] S. Rachel, I. Göthel, D. P. Arovas, and M. Vojta, Strain-Induced Landau Levels in Arbitrary Dimensions with an Exact Spectrum, Phys. Rev. Lett. **117**, 266801 (2016).
[79] M. O. Goerbig, Electronic properties of graphene in a strong magnetic field, Rev. Mod. Phys. **83**, 1193 (2011).
[80] M. Creutz, Four-dimensional graphene and chiral fermions, J. High Energy Phys. 04 (2008) 017.
[81] L. B. Drissi, E. H. Saidi, and M. Bousmina, Four-dimensional graphene, Phys. Rev. D **84**, 014504 (2011).
[82] R. Takahashi and S. Murakami, Completely flat bands and fully localized states n surfaces of anisotropic diamond-lattice models, Phys. Rev. B **88**, 235303 (2013).
[83] F. de Juan, M. Sturla, and M. A. H. Vozmediano, Space Dependent Fermi Velocity in Strained Graphene, Phys. Rev. Lett. **108**, 227205 (2012).
[84] Z. F. Ezawa, *Quantum Hall Effects. Field Theoretical Approach and Related Topics*, 2nd ed. (World Scientific, Singapore, 2008).
[85] J. Deng, H. Dong, C. Zhang, Y. Wu, J. Yuan, X. Zhu, F. Jin, H. Li, Z. Wang, H. Cai, C. Song, H. Wang, J. Q. You, and D. W. Wang, Observing the quantum topology of light, Science **378**, 966 (2022).
[86] C. Poli, J. Arkinstall, and H. Schomerus, Degeneracy doubling and sublattice polarization in strain-induced pseudo-Landau levels, Phys. Rev. B **90**, 155418 (2014).
[87] H. Shapourian, T. L. Hughes, and S. Ryu, Viscoelastic response of topological tight-binding models in two and three dimensions, Phys. Rev. B **92**, 165131 (2015).
[88] See Supplemental Material at http://link.aps.org/supplemental/10.1103/PhysRevB.108.085113 for a detailed derivation of the strain-induced PVP and PMF and relationship between the tetraxial strain and Eq. (5), which includes Ref. [89].
[89] G. R. Liu and S. S. Quek, *The Finite Element Method: A Practical Course* (Butterworth-Heinemann, Oxford, 2013).
[90] T. Low and F. Guinea, Strain-induced pseudomagnetic field for novel graphene electronics, Nano Lett. **10**, 3551 (2010).
[91] Y. Chang, T. Albash, and S. Haas, Quantum Hall states in graphene from strain-induced nonuniform magnetic fields, Phys. Rev. B **86**, 125402 (2012).
[92] Y. Jiang, T. Low, K. Chang, M. I. Katsnelson, and F. Guinea, Generation of Pure Bulk Valley Current in Graphene, Phys. Rev. Lett. **110**, 046601 (2013).
[93] B. Roy, Z. X. Hu, and K. Yang, Theory of unconventional quantum Hall effect in strained graphene, Phys. Rev. B **87**, 121408(R) (2013).
[94] Y. H. Ho, E. V. Castro, and M. A. Cazalilla, Haldane model under nonuniform strain, Phys. Rev. B **96**, 155446 (2017).
[95] É. Lantagne-Hurtubise, X. X. Zhang, and M. Franz, Dispersive Landau levels and valley currents in strained graphene nanoribbons, Phys. Rev. B **101**, 085423 (2020).
[96] X. Wen, C. Qiu, Y. Qi, L. Ye, M. Ke, F. Zhang, and Z. Liu, Acoustic Landau quantization and quantum-Hall-like edge states, Nat. Phys. **15**, 352 (2019).
[97] Z. Q. Bao, J. W. Ding, and J. Qi, Complex Landau levels and related transport properties in the strained zigzag graphene nanoribbons, Phys. Rev. B **107**, 125411 (2023).

[98] D. W. Wang, H. Cai, R. B. Liu, and M. O. Scully, Mesoscopic Superposition States Generated by Synthetic Spin-Orbit Interaction in Fock-State Lattices, Phys. Rev. Lett. **116**, 220502 (2016).

[99] J. Yuan, C. Xu, H. Cai, and D. W. Wang, Gap-protected transfer of topological defect states in photonic lattices, APL Photonics **6**, 030803 (2021).

[100] J. Yuan, H. Cai, C. Wu, S. Y. Zhu, R. B. Liu, and D. W. Wang, Unification of valley and anomalous Hall effects in a strained lattice, Phys. Rev. B **104**, 035410 (2021).

[101] K. von Klitzing, T. Chakraborty, P. Kim, V. Madhavan, X. Dai, J. Mclver, Y. Tokura, L. Savary, D. Smirnova, A. M. Rey, C. Felser, J. Gooth, and X. L. Qi, 40 years of the quantum Hall effect, Nat. Rev. Phys. **2**, 397 (2020).

[102] M. Lohse, C. Schweizer, H. Price, O. Zilberberg, and I. Bloch, Exploring 4D quantum Hall physics with a 2D topological charge pump, Nature (London) **553**, 55 (2018).

[103] O. Zilberberg, S. Huang, J. Guglielmon, M. Wang, K. P. Chen, Y. E. Kraus, and M. Rechtsman, Photonic topological boundary pumping as a probe of 4D quantum Hall physics, Nature (London) **553**, 59 (2018).

[104] V. V. Albert, L. I. Glazman, and L. Jiang, Topological Properties of Linear Circuit Lattices, Phys. Rev. Lett. **114**, 173902 (2015).

[105] J. Bao, D. Zou, W. Zhang, W. He, H. Sun, and X. Zhang, Topoelectrical circuit octupole insulator with topologically protected corner states, Phys. Rev. B **100**, 201406(R) (2019).

[106] S. Liu, S. Ma, Q. Zhang, L. Zhang, C. Yang, O. You, W. Gao, Y. Xiang, T. J. Cui, and S. Zhang, Octupole corner state in a three-dimensional topological circuit, Light Sci. Appl. **9**, 145 (2020).

[107] H. Xue, Y. Ge, H. X. Sun, Q. Wang, D. Jia, Y. J. Guan, S. Q. Yuan, Y. Chong, and B. Zhang, Observation of an acoustic octupole topological insulator, Nat. Commun. **11**, 2442 (2020).

[108] M. Weiner, X. Ni, M. Li, A. Alù, and A. B. Khanikaev, Demonstration of a third- order hierarchy of topological states in a three-dimensional acoustic metamaterial, Sci. Adv. **6**, eaay4166 (2020).

[109] F. Zhai, X. Zhao, K. Chang, and H. Q. Xu, Magnetic barrier on strained graphene: A possible valley filter, Phys. Rev. B **82**, 115442 (2010).

[110] A. Chaves, L. Covaci, Kh. Yu. Rakhimov, G. A. Farias, and F. M. Peeters, Wave-packet dynamics and valley filter in strained graphene, Phys. Rev. B **82**, 205430 (2010).

[111] Z. Wu, F. Zhai, F. M. Peeters, and H. Q. Xu, and K. Chang, Valley-Dependent Brewster Angles and Goos-Hänchen Effect in Strained Graphene, Phys. Rev. Lett. **106**, 176802 (2011).

[112] M. M. Grujić, M. Ž. Tadić, and F. M. Peeters, Spin-Valley Filtering in Strained Graphene Structures with Artificially Induced Carrier Mass and Spin-Orbit Coupling, Phys. Rev. Lett. **113**, 046601 (2014).

[113] M. Settnes, S. R. Power, M. Brandbyge, and A. Jauho, Graphene Nanobubbles as Valley Filters and Beam Splitters, Phys. Rev. Lett. **117**, 276801 (2016).